

Implicit Large-Eddy Simulation of 2D Counter-Rotating Vertical-Axis Wind Turbines

Samuel Kanner*, Luming Wang[†] and Per-Olof Persson[‡]

University of California, Berkeley, Berkeley, CA 94720-3840, U.S.A.

Recent theoretical and experimental work has suggested that placing a vertical-axis wind turbine near a similar turbine that is rotating in the opposite direction may improve the efficiency of both turbines. A high-order Implicit Large Eddy Simulations (ILES) method is used to confirm these results by modeling a 2D cross-section of the wind turbines. In order to account for the moving domain, an element flipping technique is employed. This approach flips elements and uses an \mathcal{L}^2 -projection on the interfaces between the rotating turbines and the static outer mesh region. An Arbitrary-Lagrangian-Eulerian method is used to solve for the dynamic pressure and shear stress on the turbine blades using an isentropic formulation of the compressible Navier-Stokes equation. Our preliminary results seem to confirm those of the recently published experiments for straight-bladed, counter-rotating turbines. When the turbines are oriented such that a line connecting their centers of rotation is perpendicular to the incident wind direction, the power coefficient of each turbine can increase by more than 10%. In fact, when the turbines are oriented in a doublet-like configuration, where the blades travel upwind in the interior region between the turbines, our simulations show that the power coefficient of each turbine is increased by 15%. However, unlike the experimental results, when the incident wind is oriented parallel to this line, the power coefficient of the shadowed turbine is reduced significantly. We show snapshots of the fluid velocity and hypothesize why the power of the turbines may be increased due to blockage effects. That is, at certain azimuthal angles the relative wind speed that the blade encounters is larger than in the isolated case.

I. Introduction

Vertical-axis wind turbines (VAWTs) fell out of favor during the development of the wind energy industry at the end of the twentieth century due to their inferior efficiency, reliability and structural integrity as compared to their horizontal-axis counterparts. As the popularity of floating wind turbines continue to grow (see recent publications such as Refs. 1, 2, 3, 4) researchers are re-examining ways of improving the efficiency of vertical-axis wind turbines. One such method, which was first theorized by Refs. 5 and 6, is to use counter-rotating vertical-axis wind turbines. More recently, an experimental wind farm showed that by using counter-rotating turbines, the energy extraction per planform area could be increased by a factor of ten.⁷ Interestingly, the experimental data did not show a ‘wake effect’ when one turbine was placed directly downwind of its counterpart.

By placing two, counter-rotating turbines on a single floating platform, the torque on the platform can be controlled such that a taut mooring system is no longer necessary to take off power.⁴ Furthermore, these turbines have lower centers of gravity than their horizontal-axis counterparts, which make them inherently more stable. In Ref. 4, we theorize that if multi-MW VAWTs can be proven to operate reliably for the normal lifetime of a power plant (20-25 years, usually), then the cost of floating offshore wind technologies may be reduced drastically. Counter-rotating turbines, however, break the circumferential symmetry of a

*Ph.D. Candidate, Department of Mechanical Engineering, University of California, Berkeley, Berkeley CA 94720. E-mail: kanners@berkeley.edu. AIAA Student Member.

[†]Ph.D. Candidate, Department of Mathematics, University of California, Berkeley, Berkeley CA 94720. E-mail: lwang@math.berkeley.edu. AIAA Student Member.

[‡]Associate Professor, Department of Mathematics, University of California, Berkeley, Berkeley CA 94720-3840. E-mail: persson@berkeley.edu. AIAA Senior Member.

single vertical-axis wind turbine, which makes it insensitive to the incident wind direction. Due to this asymmetry, we expect there to be certain favorable wind directions where the power from the turbines is maximized. The results from the *onshore* experimental wind farm show that, indeed, there is a favorable wind direction, which leads to a great power output of the turbines. For turbines on a floating platform, their orientation relative to the incident wind direction can more easily be changed in response to the changing incident wind conditions. We speculate that for the power to be optimized, the wind turbines need to be oriented properly, or else one turbine will be directly in the wake of the other.

The paper is organized as follows. First, we describe the ILES method and discretization techniques we used to numerically recreate the 2-bladed VAWT tested by Strickland in Ref. 8. We describe the ‘element-flipping’ technique that is used to take into account the moving interfaces in the domain between the two turbines and the static outer mesh. We show how the power coefficients of the turbines vary as a function of the incident wind direction and other parameters, such as the turbine spacing distance. We conclude with a discussion on how we believe the power is increased due to a blockage effect of the spinning turbines.

II. Mathematical Model

II.A. Governing Equations

Our simulations are based on an artificial compressibility formulation of the Navier-Stokes equations, which can approximate nearly incompressible flows well.⁹ The governing equations are derived from the compressible equations by introducing an *artificial equation of state*,¹⁰ which we define by an isentropic assumption defined in terms of an *artificial Mach number* M . The resulting compressibility effects can be shown to scale as $O(M^2)$, and with some assumptions the solution approaches the incompressible case as M goes to zero. This results in a system of equations in the conserved variables ρ (density) and $\rho\mathbf{u}$ (momentum). We impose two types of boundary conditions, free-stream flow (far field) and prescribed velocity (wall).

II.B. Model Turbine

The VAWT chosen for this study was the one built and tested by Strickland and reported in Ref. 11 as well as in Ref. 8. Since the model VAWT was actually tested in a tow-tank, the average chord Reynolds number for turbine blades is approximately $40 \cdot 10^3$. A schematic of the experimental test setup is shown in Fig. 1. The width of the tow tank was 5 m, so the effect of the side walls on the turbine blades is negligible. However, the bottom of the blades were only approximately 35 cm away from the bottom of the tank, so the proximity of this boundary on the blades could have a significant effect on the flow around the blades. The physical parameters of the VAWT are shown in Table 1. The definitions of these parameters as well as

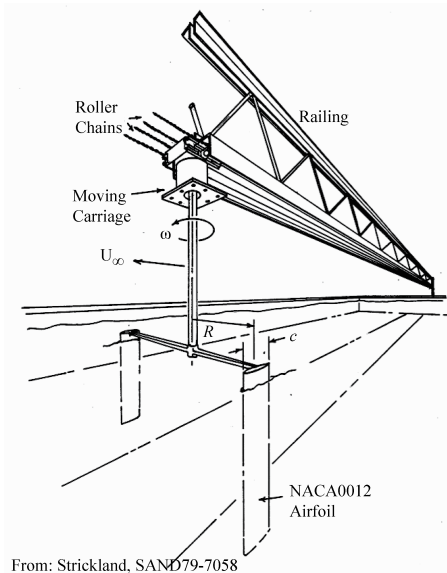


Figure 1. Schematic of tow tank experiment of low Re VAWT performed by Strickland in Ref. 11 and 8.

the definition of the azimuthal angle used for this study are shown in Fig. 2, where the 2-bladed VAWT is shown in plan view. The tip speed ratio $\lambda = \omega_1 R / U_\infty$ was fixed at 5.0 for this study. The tip speed ratio is defined as the ratio of the speed of the blade relative to the incident wind speed U_∞ . In Ref. 11, the authors do not explicitly report the blade offset distance c_0 as a percentage of the total chord length c , which is the distance from the leading edge of the airfoil to the blade mounting point, along the chord line of the airfoil. However, from the discussion on pages 57 and 59 of 11 on the measurement of the moment about the quarter-chord, we infer that $c_0 = c/4$. From this section, we also infer that the intended blade offset pitch angle α_0 , as shown in Fig. 2, to be 0° . Yet, the authors report uncertainty in the measurement of the azimuthal angle on the order of 1° . The determination of the actual α_0 used in the experiments is discussed in Ref. 12. We chose the static ‘toe-out’ angle of each of the airfoils α_0 to be 2° , since it best matches the experimental data.

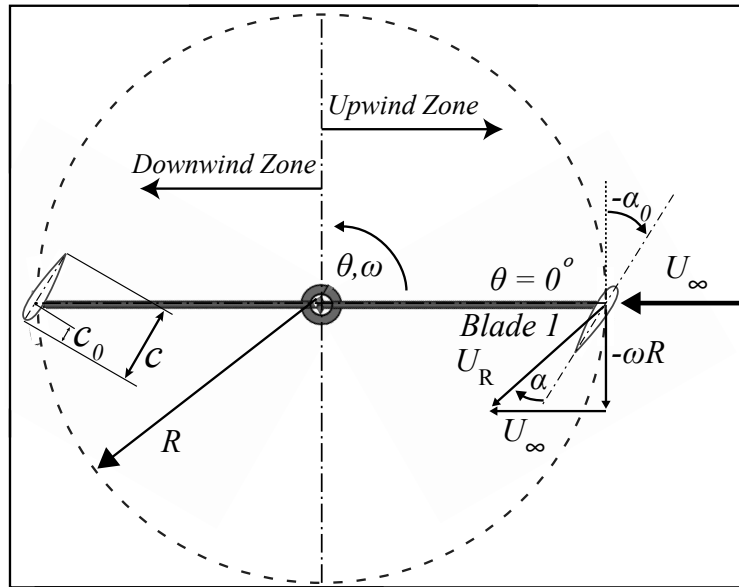


Figure 2. Plan view of 2-bladed VAWT with definitions of angle of attack α , blade offset pitch angle α_0 , chord length c , blade offset distance c_0 , VAWT radius R , azimuthal angle θ , and VAWT angular velocity ω_1 .

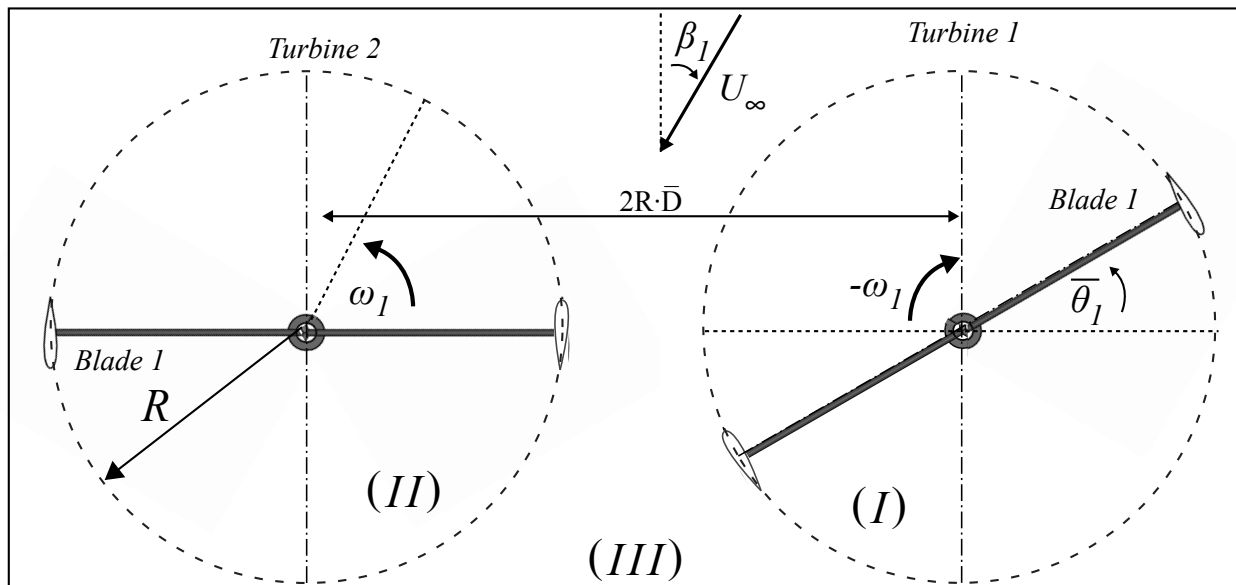
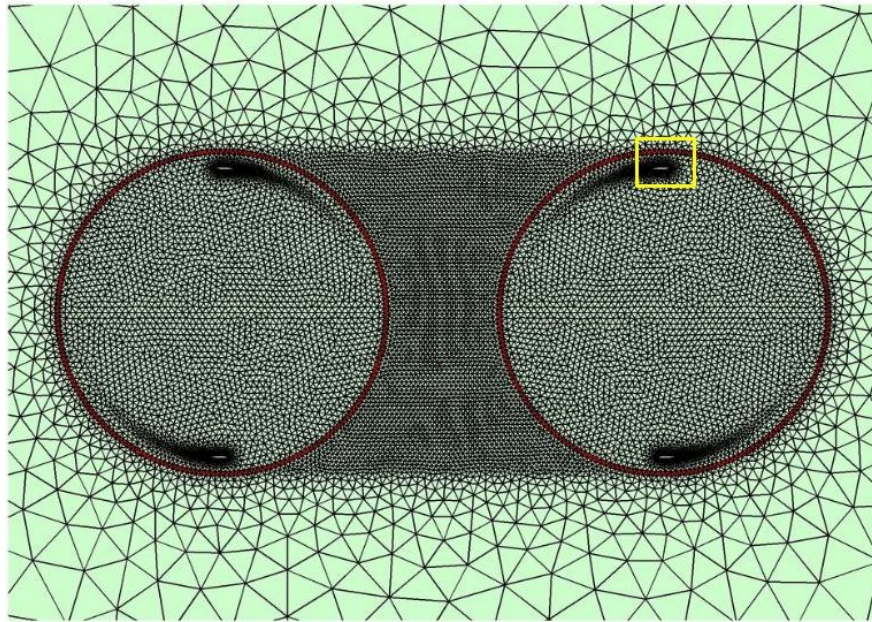


Figure 3. Plan view of counter-rotating VAWTs with definitions of VAWT radius R , azimuthal angular offset $\bar{\theta}_1$, and normalized distance \bar{D} .

Parameter	Value	Unit
c	9.14	cm
R	61.0	cm
λ	5	-
α_0	-2	deg
c_0	$0.25c$	cm

Table 1. Geometry and turbine parameters for the VAWT simulated in this study.

III. Numerical Approach



The initial spatial mesh at $t = 0.0$

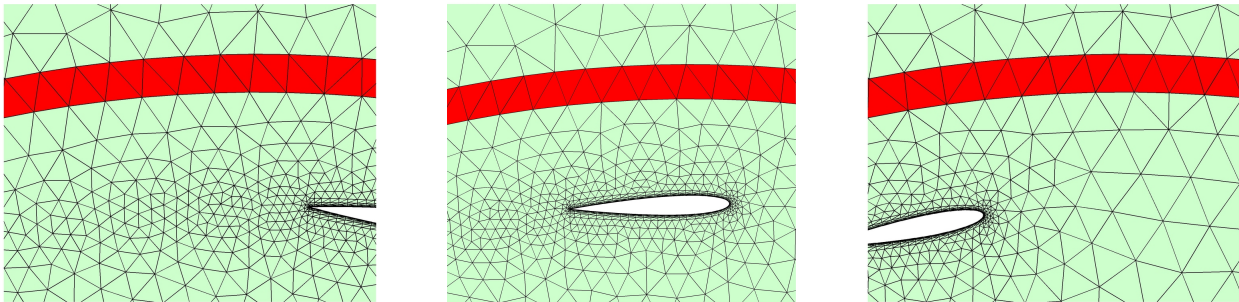


Figure 4. The unstructured triangular mesh for the double VAWT simulations. The initial mesh is showed on the top, where all the edge flipping operations happen in the area colored in red. To illustrate the mesh motion, three zoom-in plots are shown at the bottom for the area circled by a yellow window in the top plot.

III.A. Computational Domain and Moving Mesh Strategy

We use an unstructured triangular mesh for the physical domain, see Fig. 4. A hybrid structured approach is used to form the boundary layer elements around the airfoils. The rest of the computational mesh is fully unstructured and is generated using the DistMesh mesh generator.¹³ We use a slight refinement of the elements in the area behind the trailing edge of the airfoils in order to improve the resolution. In addition, as

high-order methods require meshes with curved boundaries, we use the elasticity-based approach proposed in Ref. 14 to produce well-shaped meshes with globally curved elements.

As the two turbines rotate, the mesh has to be moved accordingly. However, since the turbines rotate individually around their center axes, we cannot simply rotate the entire mesh like was done in the single turbine case in Ref. 12. Instead, we use the following moving-mesh strategy that incorporates rigid rotations that stretch the elements as well as techniques to change the element connectivities to prevent poor element qualities. First, we partition the mesh into three parts – two circular meshes around the two turbines and one rectangular mesh with two holes for the rest of the outside area. The two circular meshes are rigidly rotated according to the motion of the two wind turbines, and the outer mesh remains static. To glue all these parts together, we connect the boundary nodes of each part together and form two intermediate layers of triangular elements (the area colored in red in Fig. 4). Due to the rigid rotations, the elements in these intermediate layers will become stretched and eventually inverted without connectivity changes. To address this problem, at each time step we update the mesh connectivity in the intermediate layers by edge flipping operations.¹⁵ As shown in Fig. 5, we consider a pair of adjacent triangles where at least one of them has an unsatisfactory element quality. We then flip their shared edge and produce two new triangles sharing the new edge but with better element qualities. During each time step, we can perform this operation multiple times until the quality of all the elements in the intermediate layers are above a certain threshold.

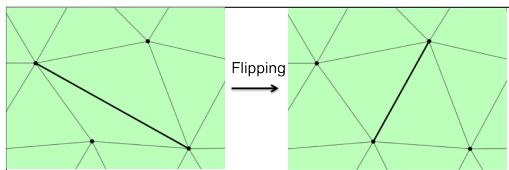


Figure 5. A local topology change for two adjacent triangles (a so-called element flip), which improves the quality of the elements.

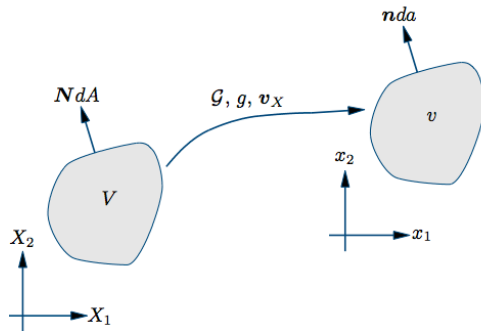


Figure 6. The mapping between the reference domain and the physical domain in the ALE framework.

III.B. Arbitrary-Lagrangian-Eulerian (ALE) Framework

For the turbine simulations, we account for the moving and deforming domains by the mapping-based Arbitrary Lagrangian-Eulerian (ALE) formulation proposed in Ref. 16. As illustrated in Fig. 6, we denote the time-varying domain as $\mathbf{v}(t) \in \mathbb{R}^n$ and consider the governing equations of the compressible isentropic flow in $\mathbf{v}(t)$ as a system of conservation laws,

$$\frac{\partial \mathbf{u}}{\partial t} + \nabla \cdot \mathbf{f}(\mathbf{u}, \nabla \mathbf{u}) = 0 \quad (1)$$

where \mathbf{u} is the vector of conserved variables and \mathbf{f} is the flux function.

The ALE formulation then chooses a fixed reference domain as V , and constructs a smooth mapping $\mathcal{G}(\mathbf{X}, t) : V \rightarrow \mathbf{v}(t)$ between the reference domain and the moving domain. Based on this mapping, we define the deformation gradient \mathbf{G} , mapping velocity \mathbf{v}_X and mapping Jacobian g as

$$\mathbf{G} = \nabla_X \mathcal{G}, \quad \mathbf{v}_X = \frac{\partial \mathcal{G}}{\partial t}, \quad g = \det \mathbf{G}. \quad (2)$$

Using these quantities, we can rewrite the conservation law (1) as a new system in the domain V ,

$$\frac{\partial \mathbf{U}}{\partial t} + \nabla_{\mathbf{X}} \cdot \mathbf{F}(\mathbf{U}, \nabla_{\mathbf{X}} \mathbf{U}) = 0 \quad (3)$$

with new solution vector \mathbf{U} and new flux functions \mathbf{F} . We refer to Ref. 16 for more details on these functions and for the derivation of the transformation.

III.C. Discontinuous Galerkin Discretization

Next, we introduce our numerical discretization for equation 3 in the reference domain, which is based on a nodal Discontinuous Galerkin (DG) method. A standard procedure¹⁷ is used for the viscous terms, where the system is split into a first-order system of equations:

$$\frac{\partial \mathbf{U}}{\partial t} - \nabla_{\mathbf{X}} \cdot \mathbf{F}(\mathbf{U}, \mathbf{q}) = 0 \quad (4)$$

$$\nabla_{\mathbf{X}} \mathbf{U} = \mathbf{q}. \quad (5)$$

Next we introduce a conforming triangulation $\mathcal{T}^h = \{K\}$ of the computational domain \mathbf{V} into elements K . On \mathcal{T}^h , we define the broken spaces \mathcal{V}_T^h and Σ_T^h as the spaces of functions whose restriction to each element K are polynomial functions of degree at most $p \geq 1$,¹⁸

$$\mathcal{V}_T^h = \{\mathbf{v} \in [L^2(\bar{\mathcal{D}})]^m \mid \mathbf{v}|_K \in [\mathcal{P}_p(K)]^m \quad \forall K \in \mathcal{T}^h\}, \quad (6)$$

$$\Sigma_T^h = \{\boldsymbol{\sigma} \in [L^2(\bar{\mathcal{D}})]^{m \times n} \mid \boldsymbol{\sigma}|_K \in [\mathcal{P}_p(K)]^{m \times n} \quad \forall K \in \mathcal{T}^h\} \quad (7)$$

where n is the spatial dimension, m is the number of solution components, and $\mathcal{P}_p(K)$ denotes the space of polynomials of degree at most $p \geq 1$ on K . Then the DG formulation for equations (4) and (5) becomes: find $\mathbf{U}^h \in \mathcal{V}_T^h$ and $\mathbf{q}^h \in \Sigma_T^h$ such that for each $K \in \mathcal{T}^h$, we have

$$\begin{aligned} \int_K \frac{\partial \mathbf{U}^h}{\partial t} \cdot \mathbf{v}^h dx - \int_K \mathbf{F}^{\text{inv}}(\mathbf{U}^h) : \nabla_{\mathbf{X}} \mathbf{v}^h dx + \oint_{\partial K} (\widehat{\mathbf{F}^{\text{inv}} \cdot \mathbf{n}}) \cdot \mathbf{v}^h ds \\ = - \int_K \mathbf{F}^{\text{vis}}(\mathbf{U}^h, \mathbf{q}^h) : \nabla_{\mathbf{X}} \mathbf{v}^h dx + \oint_{\partial K} (\widehat{\mathbf{F}^{\text{vis}} \cdot \mathbf{n}}) \cdot \mathbf{v}^h ds, \quad \forall \mathbf{v}^h \in \mathcal{V}_T^h \end{aligned} \quad (8)$$

$$\int_K \mathbf{q}^h : \boldsymbol{\sigma}^h dx = - \int_K \mathbf{U}^h \cdot (\nabla_{\mathbf{X}} \cdot \boldsymbol{\sigma}^h) dx + \oint_{\partial K} (\widehat{\mathbf{U}^h \otimes \mathbf{n}}) : \boldsymbol{\sigma}^h ds, \quad \forall \boldsymbol{\sigma}^h \in \Sigma_T^h. \quad (9)$$

Here, we have split the flux function into an inviscid and a viscous part according to $\mathbf{F}(\mathbf{U}, \nabla_{\mathbf{X}} \mathbf{U}) = \mathbf{F}^{\text{inv}}(\mathbf{U}) + \mathbf{F}^{\text{vis}}(\mathbf{U}, \nabla_{\mathbf{X}} \mathbf{U})$. For the numerical fluxes in the boundary integrals, we use Roe's method¹⁹ to approximate the inviscid flux and we treat the viscous flux using the Compact Discontinuous Galerkin (CDG) method.²⁰ From equations (8) and (9), a non-linear semi-discrete system is assembled using a standard finite element approach, which we solve using a parallel high-order diagonally implicit Runge-Kutta (DIRK) solver.²¹

III.D. Local \mathcal{L}^2 -Projections

The ALE framework relies on the mapping $\mathcal{G}(\mathbf{X}, t)$ being smooth, which is only possible if the mesh can be moved without connectivity changes. To allow for the frequent element edge flips in our moving-mesh strategy, we employ the \mathcal{L}^2 -projection strategy proposed in Ref. 15 to locally interpolate the solutions between the old and the new meshes.

It is clear that each local edge flip replaces two old elements by two new elements. Denote the old pair by $\{K_1, K_2\}$ and the new pair by $\{\tilde{K}_1, \tilde{K}_2\}$, see Fig. 7. We can easily form the 4 sub-triangles $\{\tilde{K}_1 \cap K_1, \tilde{K}_1 \cap K_2, \tilde{K}_2 \cap K_1, \tilde{K}_2 \cap K_2\}$ by finding the edge intersections. Suppose $\{\phi_1^i, \phi_2^i, \dots, \phi_N^i\}$ are basis functions of the old element K_i and $\{\tilde{\phi}_1^i, \tilde{\phi}_2^i, \dots, \tilde{\phi}_N^i\}$ are basis functions of the new element \tilde{K}_i . Write the numerical solution \mathbf{U}^h as a linear combination of the basis functions of the old element K_i as

$$\mathbf{U}^h = \sum_{j=1}^N \mathbf{U}_j^i \phi_j^i. \quad (10)$$

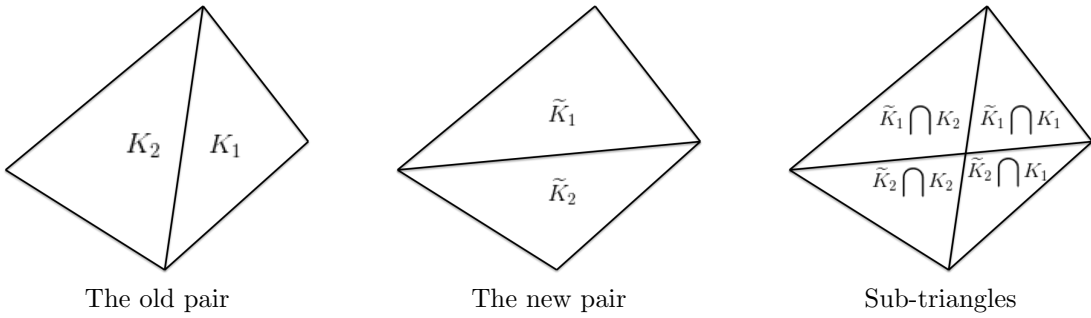


Figure 7. Local element splitting for edge flips.

The \mathcal{L}^2 -projection then computes an approximate solution \tilde{U}^h to U^h on the new element \tilde{K}_i as

$$\tilde{U}^h = \sum_{j=1}^{\tilde{N}} \tilde{U}_j^i \tilde{\phi}_j^i, \quad (11)$$

by solving the linear system

$$M \begin{bmatrix} \tilde{U}_1^i \\ \tilde{U}_2^i \\ \vdots \\ \tilde{U}_{\tilde{N}}^i \end{bmatrix} = P^1 \begin{bmatrix} U_1^1 \\ U_2^1 \\ \vdots \\ U_N^1 \end{bmatrix} + P^2 \begin{bmatrix} U_1^2 \\ U_2^2 \\ \vdots \\ U_N^2 \end{bmatrix} \quad (12)$$

where

$$M_{j,k} = \int_{\tilde{K}_i} \tilde{\phi}_k^i \tilde{\phi}_j^i dx, \quad P_{j,k}^1 = \int_{\tilde{K}_i \cap K_1} \phi_k^1 \tilde{\phi}_j^i dx, \quad P_{j,k}^2 = \int_{\tilde{K}_i \cap K_2} \phi_k^2 \tilde{\phi}_j^i dx. \quad (13)$$

Equation 12 can be solved for \tilde{U}^h and used as the transferred solution to resume the time-stepping process on the new mesh. The details on this derivation can be found in Ref. 15.

Our combined method for the moving-mesh strategy, ALE framework, DG scheme and local \mathcal{L}^2 -projection is summarized in algorithm 1.

Algorithm 1 Discontinuous Galerkin ALE Method with Local \mathcal{L}^2 -Projections

Require: Triangulation \mathcal{T}^h and initial solution U^{h,t_0} at t_0

Require: Time step Δt and mesh quality threshold δ

Ensure: Solution U^{h,t_i} for each time step t_i until time T

while $t_0 < t_i \leq T$ **do**

 Rigidly rotate the two circular meshes

 Compute deformation gradient G , mapping velocity \mathbf{v} and mapping Jacobian g

 Solve U^{h,t_i} by the DG method with the ALE framework

if min quality of $K \in \mathcal{T}^h < \delta$ **then**

 Create $\tilde{\mathcal{T}}^h$ by local element flipping

 Solve for \tilde{U}^{h,t_i} by local \mathcal{L}^2 -projections

$\mathcal{T}^h \leftarrow \tilde{\mathcal{T}}^h$

$U^{h,t_i} \leftarrow \tilde{U}^{h,t_i}$

end if

end while

IV. Results

To explore the efficiency of the turbines the tangential force on each airfoil of the turbines is calculated. The sectional tangential force coefficient is usually defined as,

$$C_{T,i}^j(\theta) = \frac{F_{T,i}^j(\theta)}{1/2\rho U_\infty^2 c} \quad (14)$$

where $F_{T,i}^j$ is the sectional tangential force of the i^{th} blade on the j^{th} turbine, with $i = 1, \dots, N_b$ and $j = 1, 2$. For a straight-bladed VAWT, the power coefficient of the j^{th} turbine C_p^j is a function of the average of the tangential force coefficient over one revolution, \bar{C}_T^j and other parameters, such that

$$C_p^j = \sum_{i=1}^{N_b} \frac{\frac{\omega}{2\pi} \int_0^{2\pi} F_{T,i}^j(\theta) R d\theta}{1/2\rho U_\infty^3 2R} = \sum_{i=1}^{N_b} \frac{\lambda \bar{C}_{T,i}^j c}{2} \frac{c}{R} \quad (15)$$

In the following section we define an average power coefficient for the turbine pair as

$$C_p^* = \frac{C_p^1 + C_p^2}{2\bar{C}_p} \quad (16)$$

where \bar{C}_p is the average power coefficient of an isolated turbine. To calculate this baseline value, the rotational speed of one of the turbines is set to null, such that $\dot{\theta}_2 = 0$ and ran the same simulations. Varying which turbine was frozen and the incident wind direction resulted in less than 5% variation of the power coefficient of the isolated turbine.

IV.A. Parameter Study

In order to maximize the synergistic effect, the distance between the centers of rotation of the turbines $2R\bar{D}$ was varied to determine the optimal distance between the turbines. The results of this parameter study are shown in Fig. 8.

The circumferential direction represents the direction the incident wind originates from. The radial direction represents the normalized power coefficient C_p^* . For $\beta_1 = 90^\circ, 270^\circ$, $C_p^* < 0$ due to the shadowing effect from the upwind turbine, which can be seen in Fig. 11, as well. This effect was not seen in the experimental study reported in,⁷ who even saw a slight jump in the efficiency around $\beta_1 = 105^\circ$ (which is 195° in their figure since their orientation of β_1 is offset by 90°).

We use the vocabulary developed for counter-rotating cylinders studied in 22, such that when the wind comes from the ‘North’ ($\beta_1 = 0^\circ$) the configuration is ‘doublet-like’, while when the wind comes from the ‘South’ ($\beta_1 = 180^\circ$), it is ‘reverse doublet-like’. From Fig. 8, it is clear that the turbines are most efficient in the ‘doublet-like’ configuration, gaining nearly 30% total power from their isolated counterparts. This synergistic effect is almost as large in the ‘reverse doublet-like’ configuration.

In Ref. 4, the turbines are forced to counter-rotate at the same speed using a timing belt system, to control the platform orientation. Thus, the angular offset of the turbines, denoted as $\bar{\theta}_1$ and portrayed in Fig. 3, is fixed in time. Figure 9 shows the variation of the average power coefficient when the angular offset of the turbines is changed to 30° and 90° . The plot shows that the power coefficient is fairly insensitive to this variation.

IV.B. Flow Structure

To further explore the results, we can visualize the fluid velocity at certain time instants $\vec{U} = [u, v]$. Figure 11 shows a time instance of the domain with the color representing the magnitude of the fluid velocity in the direction of the incident wind speed. Clearly, the flow is accelerated between the turbines by over 50%.

$$u^*(\vec{x}, t) = \frac{\vec{U}(\vec{x}, t) \cdot \vec{\beta}_1}{|U_\infty|} \quad (17)$$

However, when β_1 is orthogonal to the orientation of the platforms, the upstream turbine retards the incident flow to such a degree that the power produced by the downstream turbine is actually negative, which means that the turbine needs power to spin. Hence, the polar plots in Figs. 8 and 9 show negative total power produced by the turbine pair.

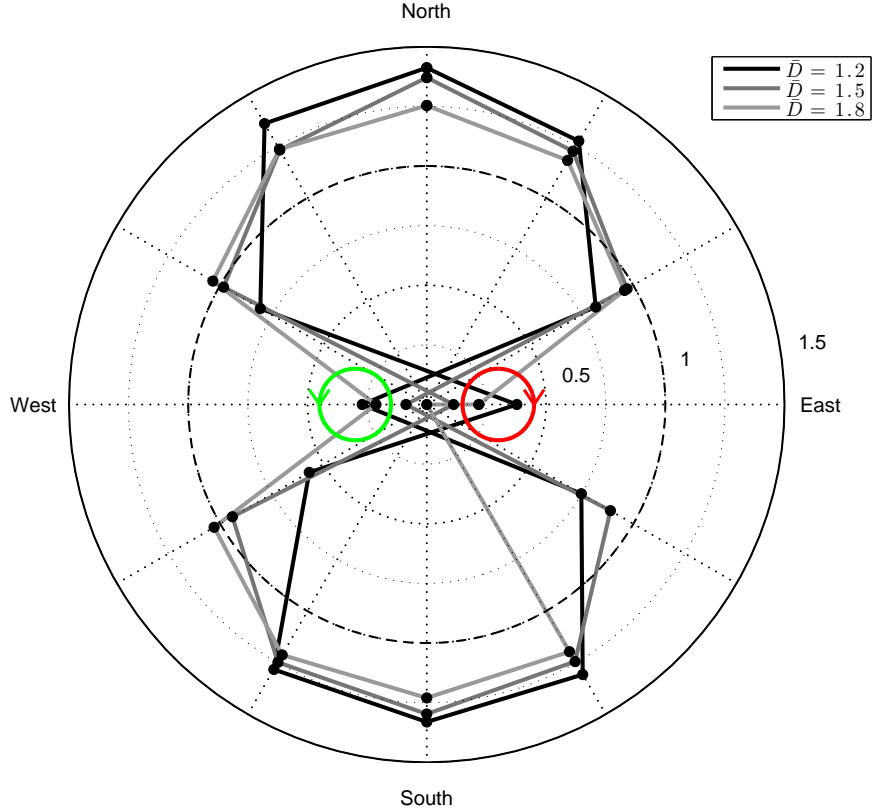


Figure 8. Average power coefficient of counter-rotating wind turbines as a function of wind direction and turbine spacing.

V. Conclusions and Future Work

To the authors' knowledge the findings presented herein represent the first preliminary study of counter-rotating vertical-axis wind turbines using high-order LES techniques. The results confirm that the synergistic effect between the counter-rotating turbines (found from previous experimental work described in 7) may be up to 25-30%. However, the optimal angle to maximize this beneficial is quite different than the one which has been previously published. We find that either the 'doublet-like' or 'reverse doublet-like' configurations are the optimal orientations for the turbines.

There are many reasons why the work here may not agree with the previously published experimental data. Namely, the simulations performed in this study were in 2D using uniform incident flow. At the experimental field site, the incident wind is certainly turbulent with a vertical variation proportional to the atmospheric boundary layer. Furthermore, under certain tip-speed ratios (for instance, $\lambda < 5$ as shown in 12), three-dimensional effects become significant. The turbines used in the experimental study were purchased from Windspire EnergyTM, who uses proprietary airfoil shapes on their turbines. Thus, an exact numerical replica could not be built.

V.A. Future Work

In the future, we hope to perform a more in-depth analysis of the flow fields and momentum fluxes to determine how the blockage effects of the turbines can cause the flow around the turbines to accelerate. We surmise that it is this accelerated flow field, which leads to an increase in the relative wind speed over certain range of azimuthal angles, that may lead to increase power production of the turbines. However, this argument would only hold for the case of a 'doublet-like' configuration. The physical mechanism for the increased power production in the 'reverse doublet-like' configuration remains an open question.

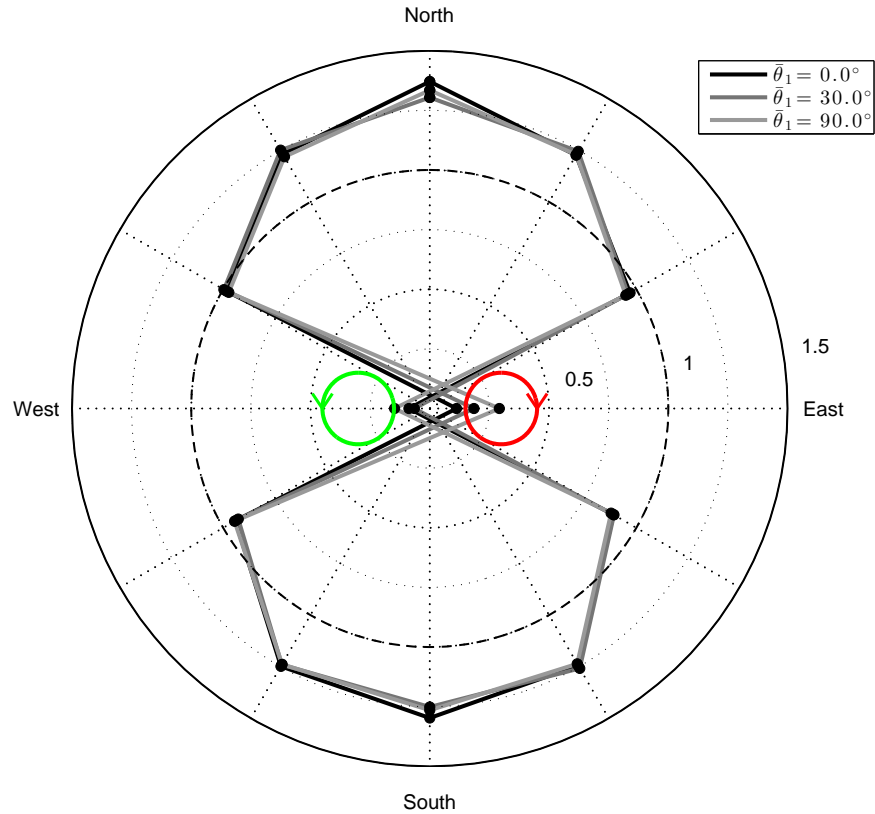


Figure 9. Average power coefficient of counter-rotating wind turbines as a function of wind direction and turbine offset angle θ_1 (see Fig. 3).

Acknowledgements

The first author was supported by the Department of Defense (DoD) through the National Defense Science & Engineering Graduate Fellowship (NDSEG) Program as well as the National Science Foundation (NSF) through the Graduate Research Fellowship Program. The first author would also like to thank his PhD adviser, Prof. R.W. Yeung. This research used resources of the National Energy Research Scientific Computing Center, a DOE Office of Science User Facility supported by the Office of Science of the U.S. Department of Energy under Contract No. KJ04-01-00-0.

References

- ¹Bull, D. L., Fowler, M., and Goupee, A., "A Comparison of Platform Options for Deep-water Floating Offshore Vertical Axis Wind Turbines: An Initial Study." Tech. rep., Sandia National Laboratories (SNL-NM), Albuquerque, NM (United States), 2014.
- ²Borg, M. and Collu, M., "A comparison between the dynamics of horizontal and vertical axis offshore floating wind turbines," *Philosophical Transactions of the Royal Society A: Mathematical, Physical and Engineering Sciences*, Vol. 373, No. 2035, 2015, pp. 20140076.
- ³Borg, M. and Collu, M., "Offshore floating vertical axis wind turbines, dynamics modelling state of the art. Part III: Hydrodynamics and coupled modelling approaches," *Renewable and Sustainable Energy Reviews*, Vol. 46, June 2015, pp. 296–310.
- ⁴Kanner, S., *Design, Analysis, Hybrid Testing and Orientation Control of a Floating Platform with Counter-Rotating Vertical-Axis Wind Turbines*, Ph.D. thesis, University of California, Berkeley, 2015.
- ⁵Paul R. Schatzle, Paul C. Klimas, and H. R. Spahr, "Aerodynamic interference between two Darrieus wind turbines." Tech. rep., Sandia National Laboratories, Albuquerque, NM, 1981.
- ⁶Rajagopalan, R. G., Klimas, P. C., and Rickerl, T. L., "Aerodynamic interference of vertical axis wind turbines," *Journal of Propulsion and Power*, Vol. 6, No. 5, 1990, pp. 645–653.
- ⁷Dabiri, J. O., "Potential order-of-magnitude enhancement of wind farm power density via counter-rotating vertical-axis wind turbine arrays," *Journal of Renewable and Sustainable Energy*, Vol. 3, 2011, pp. 043104–1:14.
- ⁸Strickland, J. H., Smith, T., and Sun, K., "Vortex Model of the Darrieus Turbine: An Analytical and Experimental Study.

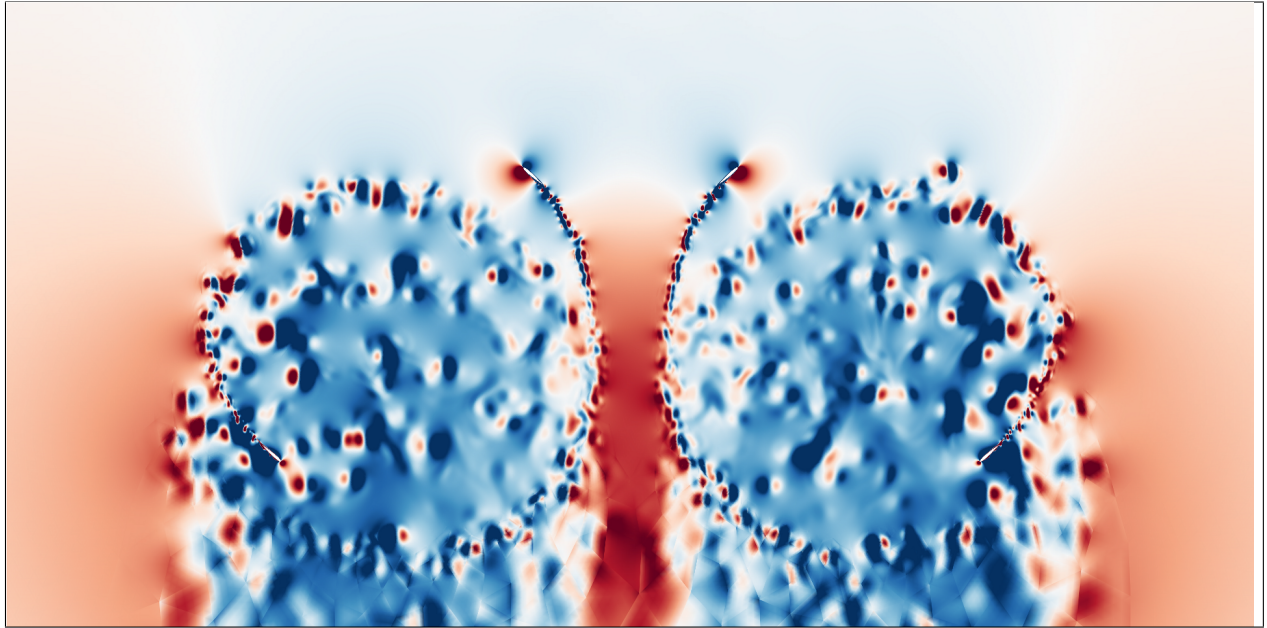


Figure 10. Snapshot of the normalized fluid speed, u^* for $\alpha_0 = 0^\circ$, $D=1.2$, $\beta_1 = 0^\circ$, $\lambda = 5.0$.

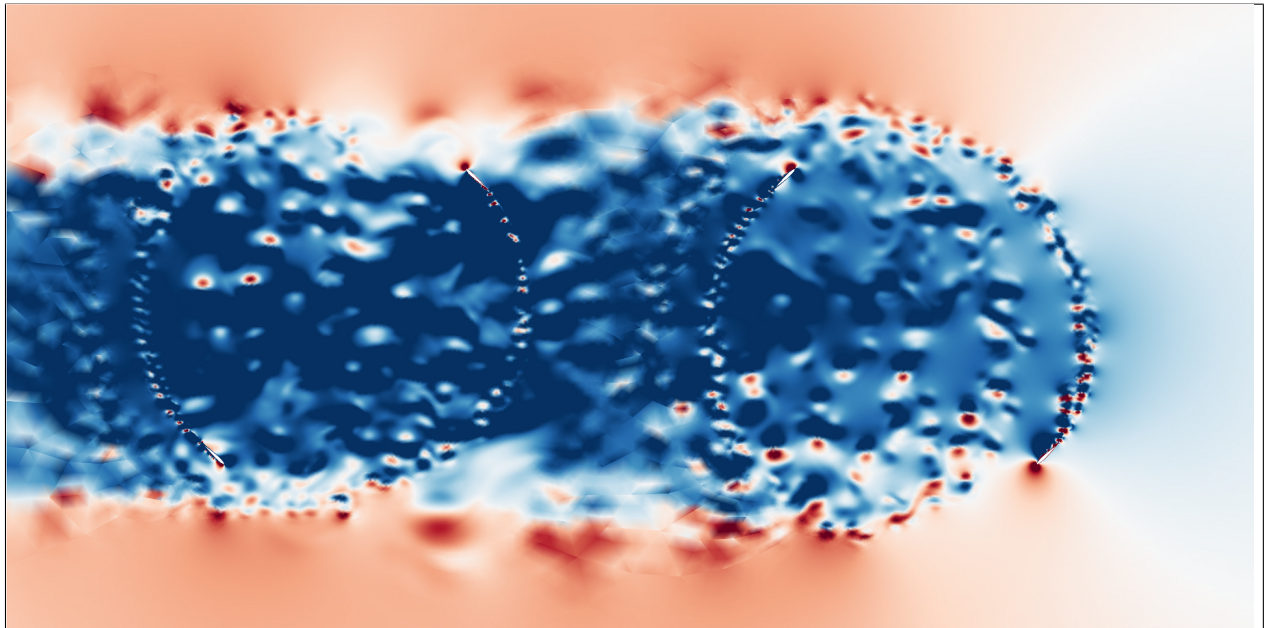


Figure 11. Snapshot of the normalized fluid speed, u^* in the direction of the incident wind $\alpha_0 = -2^\circ$, $D=1.5$, $\beta_1 = 90^\circ$, $\lambda = 5.0$.

Final Report,” Tech. Rep. SAND-81-7017, Sandia National Labs., Albuquerque, NM (USA); Oregon State Univ., Corvallis (USA). Dept. of Mechanical Engineering, June 1981.

⁹Froehle, B. M., *High-Order Discontinuous Galerkin Fluid-Structure Interaction Methods*, Ph.D. thesis, University of California, Berkeley, 2013.

¹⁰Chorin, A. J., “A numerical method for solving incompressible viscous flow problems [J. Comput. Phys. **2** (1967), no. 1, 12–36],” *J. Comput. Phys.*, Vol. 135, No. 2, 1997, pp. 115–125, With an introduction by Gerry Puckett, Commemoration of the 30th anniversary {of J. Comput. Phys.}.

¹¹Strickland, J. H., Webster, B. T., and Nguyen, T., “Vortex Model of the Darrieus Turbine: An Analytical and Experimental Study.” Tech. Rep. SAND-79-7058, Sandia National Labs., Albuquerque, NM (USA); Oregon State Univ., Corvallis (USA). Dept. of Mechanical Engineering, June 1979.

¹²Kanner, S. and Persson, P.-O., “Validation of a High-Order Large-Eddy Simulation Solver Using a Vertical-Axis Wind Turbine,” *AIAA Journal*, 2015.

¹³Persson, P.-O. and Strang, G., “A simple mesh generator in Matlab,” *SIAM Rev.*, Vol. 46, No. 2, 2004, pp. 329–345.

¹⁴Persson, P.-O. and Peraire, J., “Curved mesh generation and mesh refinement using Lagrangian solid mechanics,” *47th AIAA Aerospace Sciences Meeting and Exhibit, Orlando, Florida*, Jan. 2009, AIAA-2009-949.

¹⁵Wang, L. and Persson, P.-O., “High-order Discontinuous Galerkin Simulations on Moving Domains using an ALE Formulation and Local Remeshing with Projections,” *53rd AIAA Aerospace Sciences Meeting, Orlando, Florida*, 2015, AIAA-2015-0820.

¹⁶Persson, P.-O., Bonet, J., and Peraire, J., “Discontinuous Galerkin solution of the Navier-Stokes equations on deformable domains,” *Comput. Methods Appl. Mech. Engrg.*, Vol. 198, No. 17–20, 2009, pp. 1585–1595.

¹⁷Arnold, D. N., Brezzi, F., Cockburn, B., and Marini, L. D., “Unified analysis of discontinuous Galerkin methods for elliptic problems,” *SIAM J. Numer. Anal.*, Vol. 39, No. 5, 2001/02, pp. 1749–1779.

¹⁸Hesthaven, J. S. and Warburton, T., *Nodal discontinuous Galerkin methods*, Vol. 54 of *Texts in Applied Mathematics*, Springer, New York, 2008, Algorithms, analysis, and applications.

¹⁹Roe, P. L., “Approximate Riemann solvers, parameter vectors, and difference schemes,” *J. Comput. Phys.*, Vol. 43, No. 2, 1981, pp. 357–372.

²⁰Peraire, J. and Persson, P.-O., “The compact discontinuous Galerkin (CDG) method for elliptic problems,” *SIAM J. Sci. Comput.*, Vol. 30, No. 4, 2008, pp. 1806–1824.

²¹Persson, P.-O., “Scalable Parallel Newton-Krylov Solvers for Discontinuous Galerkin Discretizations,” *47th AIAA Aerospace Sciences Meeting and Exhibit, Orlando, Florida*, 2009, AIAA-2009-606.

²²Chan, A. S., Dewey, P. A., Jameson, A., Liang, C., and Smits, A. J., “Vortex suppression and drag reduction in the wake of counter-rotating cylinders,” *Journal of Fluid Mechanics*, Vol. 679, July 2011, pp. 343–382.